Modified DTC of a Six-Phase Induction Motor With a Second-Order Sliding-Mode MRAS-Based Speed Estimator

Mohammad Hosein Holakooie, Mansour Ojaghi, *Senior Member, IEEE*, and Asghar Taheri

***Abstract*—This paper deals with a model reference adaptive system (MRAS) estimator based on the second-order sliding-mode (SOSM) strategy for speed-sensorless direct torque control (DTC) of a six-phase induction motor. A compensated flux observer is proposed using the well-known supertwisting algorithm, which is inherently an SOSM technique. This observer is adopted as the reference model in the MRAS-based speed estimator to overcome the chattering problem of the classical sliding-mode techniques. The estimator is robust against parameter uncertainties and dc offsets. In addition, a supertwisting-algorithm-based second-order sliding-mode (ST-SOSM) controller is designed for the speed loop in the DTC strategy to increase its robustness under applying external load disturbances. The speed control loop needs the load torque signal. For this purpose, an ST-SOSM load torque observer is proposed, where it provides a robust performance without the penalty of high chattering. Simulation and experimental results confirm the validity and the effectiveness of the proposed approaches.**

***Index Terms*—Direct torque control (DTC), model reference adaptive system (MRAS), six-phase induction motor (6PIM), speed-sensorless drive, supertwisting-algorithm-based second-order sliding-mode (ST-SOSM) observer.**

I. Introduction

MULTIPHASE drive systems have a nearly 40-year history of research and study due to their promising advantages against the conventional three-phase systems. The phase redundancy of the multiphase drives provides extra merits such as open-phase fault detection and fault-tolerant operation [1]–[5], series-connected multimotor drive systems [6], asymmetry and dead-time compensation [7], and braking systems [8]. Among the multiphase drives, the six-phase induction motor (6PIM) drive is recognized as an interesting topology because of its strong mechanical construction, low maintenance requirements, and a modular three-phase structure.

Despite the numerous endeavors, speed-sensorless control of the induction motor still remains a challenging task due to the model uncertainties, disturbances, high-order dynamics, etc.

Manuscript received September 13, 2017; revised February 14, 2018; accepted April 4, 2018. Date of publication April 9, 2018; date of current version November 19, 2018. Recommended for publication by Associate Editor Y. Sozer. *(Corresponding author: Mansour Ojaghi.)*

The authors are with the Department of Electrical Engineering, University of Zanjan, Zanjan 45371-38791, Iran (e-mail:

rately in the severe conditions. The authors in [20] proposed two adaptation mechanisms based on the sliding-mode and fuzzy logic methods to resolve this problem. A sliding-mode adaptation mechanism has been presented in [21], which focuses on the chattering reduction. The primary idea of the MRAS speed estimator is based on the rotor flux [18], which suffers from instability phenomena in the low-speed regenerating region. Stability improvement in the rotor flux-based MRAS estimator in the low-speed regenerating mode has been investigated in [22] and [23]. In [23], the actual voltage signals in the reference model have been replaced by the corresponding voltage command signals to improve the low- and zero-speed operation, improve the stability of the estimator, and eliminate the voltage sensors. In [24], a reactive-power-based MRAS speed estimator has been introduced, which is stable in the regenerating mode.

The reference model in the rotor-flux-based MRAS speed estimator is affected by multiple phenomena such as the stator resistance mismatch and the dc offsets. Hence, the modification of the reference model has been proposed by several researchers. A compensated reference model against the dc offset has been introduced in [25]. A revised MRAS speed estimator for a sensorless drive of induction motors in the field-weakening region has been presented in [26]. A promising technique to reach a reliable and robust speed estimator is attained by using the sliding-mode approach. Different utilizations of the sliding-mode technique have been addressed either in the form of an observer [13], [28] or a controller [14]. A rotor-flux-based MRAS speed estimator has been recently proposed in [27], which is based on the first-order sliding-mode (FOSM) observer and is designed by the H-infinity method. The FOSM control maintains the advantages of robustness against the internal and external disturbances and the parameter uncertainties. However, this approach is totally overshadowed by undesired high-frequency oscillations within the sliding mode due to the imperfect modeling of the system, which is also referred to as chattering. By a smooth continuous approximation of the discontinuous control function, the chattering problem is mitigated [27], while the sliding surface is also reached. However, this approximation expels the sliding mode from ideal sliding and can lead to decrease of the robustness of the system [31].

Higher order sliding-mode (HOSM) control can be used to achieve an efficient solution to overcome the chattering problem along with increasing the accuracy of the state trajectories in the sliding modes and without decreasing the robustness of the system [32]. In the FOSM method, the sliding variable s is chosen such that its relative degree is 1 with respect to the system input; hence, the first-order time derivative of the sliding variable will be a function of the control input. HOSM control is based on high-order derivatives of the sliding variable. In particular, the second-order sliding-mode (SOSM) method acts on the second-order derivative of the sliding variable; hence, it is necessary to provide the signum of the time derivative of the sliding variable, i.e., sign $(\dot{s})$. This is an unfavorable feature for the SOSM because it requires more information about the system [33], [34]. This restriction is relaxed by introducing the supertwisting algorithm (STA) [32], whereby there is no need of the derivative of the sliding variable.

In this paper, a new compensated SOSM flux observer is proposed for the 6PIM based on the STA. The observer is applied as the reference model in the MRAS-based speed estimator. The objective is twofold 1) obtaining a robust MRAS-based speed estimator and 2) getting rid of the chattering problem. Furthermore, the speed control loop of the DTC is designed using a supertwisting-algorithm-based second-order sliding-mode (ST-SOSM) control strategy to provide disturbance-free operation of the DTC drive system. A load torque observer is proposed in the speed control loop, which is also based on the ST-SOSM method to ensure the robustness of the observer. It is worth mentioning that different load torque observers have been presented in the literature, which are usually based on the Kalman filter [17], the Luenberger observer [14], and the FOSM technique [35]. The Kalman filter algorithm suffers from the high computational effort, while the Luenberger observer is overshadowed by the model uncertainties. The FOSM observer improves the robustness of the estimation, but it may have a degraded performance due to the chattering problem. The proposed load torque observer alleviates the chattering problem, while maintaining the robustness and simplicity. The proposed sensorless DTC scheme is combined with a duty cycle control to reduce low-order harmonics in the stator currents. Simulation and experimental results are presented to confirm the validity and effectiveness of the proposed schemes.

II. Mathematical Model of the 6PIM

In this study, the 6PIM modeling is based on the vector space decomposition strategy [36]. According to this modeling technique, a 6PIM with near-sinusoidal distributed windings is modeled in three orthogonal subspaces, which are commonly named as $\alpha-\beta$, z_1-z_2, and o_1-o_2 subspaces. Among the subspaces, only the $\alpha-\beta$ components share useful electromechanical energy conversion, while z_1-z_2 and o_1-o_2 components cannot generate any usable electromechanical energy in the air gap and just produce losses. There are different types of 6PIM, including symmetrical or asymmetrical structures, with single or two isolated neutral points [3]. In this paper, an asymmetrical 6PIM with two neutral points is adopted. For this motor, the transfer between the normal six-phase system (i.e., $a-x-b-y-c-z$) and the decoupled orthogonal subspaces (i.e., $\alpha-\beta$, z_1-z_2, and o_1-o_2) is performed using T_6 matrix as follows [36]:

$$\boldsymbol{T}_6=\frac{1}{3}\begin{bmatrix}1 & \frac{\sqrt{3}}{2} & -\frac{1}{2} & -\frac{\sqrt{3}}{2} & -\frac{1}{2} & 0\\ 0 & \frac{1}{2} & \frac{\sqrt{3}}{2} & \frac{1}{2} & -\frac{\sqrt{3}}{2} & -1\\ 1 & -\frac{\sqrt{3}}{2} & -\frac{1}{2} & \frac{\sqrt{3}}{2} & -\frac{1}{2} & 0\\ 0 & \frac{1}{2} & -\frac{\sqrt{3}}{2} & \frac{1}{2} & \frac{\sqrt{3}}{2} & -1\\ 1 & 0 & 1 & 0 & 1 & 0\\ 0 & 1 & 0 & 1 & 0 & 1\end{bmatrix}. \quad (1)$$

The fundamental components of the 6PIM electrical quantities, including its voltages, currents, and fluxes, besides the harmonics of the order $12k\pm1, (k=1,2,3,...)$ are mapped into the $\alpha-\beta$ subspace. The harmonics of the order $6k\pm1, (k=1,3,5,...)$ are transferred into the z_1-z_2 subspace, and the zero sequence harmonics are mapped into the o_1-o_2 subspace.

The voltage equations of the 6PIM in the $\alpha-\beta$ subspace can be expressed as

$$\begin{cases} \boldsymbol{v}_s = R_s \boldsymbol{i}_s + \dot{\boldsymbol{\Psi}}_s \\ 0 = R_r \boldsymbol{i}_r + \dot{\boldsymbol{\Psi}}_r - j\omega_r \boldsymbol{\Psi}_r \end{cases} \tag{2}$$

with

$$\begin{cases} \boldsymbol{v}_s = v_{s\alpha} + jv_{s\beta} \\ \boldsymbol{i}_s = i_{s\alpha} + ji_{s\beta}, \boldsymbol{i}_r = i_{r\alpha} + ji_{r\beta} \\ \boldsymbol{\Psi}_s = \psi_{s\alpha} + j\psi_{s\beta}, \boldsymbol{\Psi}_r = \psi_{r\alpha} + j\psi_{r\beta} \end{cases} \tag{3}$$

where $\boldsymbol{i}_s$ and $\boldsymbol{i}_r$ are the stator and rotor currents, $\boldsymbol{\Psi}_s$ and $\boldsymbol{\Psi}_r$ are the stator and rotor fluxes, R_s and R_r are the stator and rotor resistances, ω_r is the electrical angular velocity, and j is the imaginary unit. The flux equations are given by

$$\begin{cases} \boldsymbol{\Psi}_s = L_s \boldsymbol{i}_s + L_m \boldsymbol{i}_r \\ \boldsymbol{\Psi}_r = L_m \boldsymbol{i}_s + L_r \boldsymbol{i}_r \end{cases} \tag{4}$$

where L_s, L_r, and L_m are the stator, rotor, and magnetizing inductances.

The voltage equations of the 6PIM in the z_1-z_2 subspace are

$$\begin{cases} v_{sz1} = R_s i_{sz1} + L_{ls} \dot{i}_{sz1} \\ v_{sz2} = R_s i_{sz2} + L_{ls} \dot{i}_{sz2} \end{cases} \tag{5}$$

where L_{ls} is the stator leakage inductance. It is worth noting that for the studied 6PIM with two neutral points, the zero-sequence currents cannot flow because it operates as two balanced three-phase systems.

The electromagnetic torque of the 6PIM is defined as

$$T_e = 3P\boldsymbol{\Psi}_s \otimes \boldsymbol{i}_s \tag{6}$$

where P is the number of the pole pairs and $\otimes$ represents the cross product.

III. Supertwisting Algorithm

Consider a dynamic system with a relative degree of 1 with respect to the sliding variable; then, the control law of the STA can be written as [34]

$$\begin{aligned} u &= -\lambda |s|^{\rho} \text{sign}\,(s) + u_1 \\ \dot{u}_1 &= \begin{cases} -u, & |u| > U_M \\ -\zeta \text{sign}\,(s), & |u| \le U_M \end{cases} \end{aligned} \tag{7}$$

where $\lambda, \zeta,$ and U_M are constant parameters, and $0 < \rho \le 0.5$. The finite-time convergence of the STA is achieved under the specified sufficient conditions, which are commonly proved in two ways. The first way is based on a geometrical technique [34], and the second way is based on the Lyapunov stability theorem [37]. In this paper, the geometrical method will be employed to ensure the finite-time convergence of the proposed ST-SOSM techniques.

Fig. 1 shows the typical STA trajectories in the phase portrait s–$\dot{s}$, for different setting parameters of the STA. As can be seen, the trajectories of the STA perform rotations around the origin while converging in a finite time to the origin $s = \dot{s} = 0$. The required condition for such a convergence of the STA will be discussed later in this study.

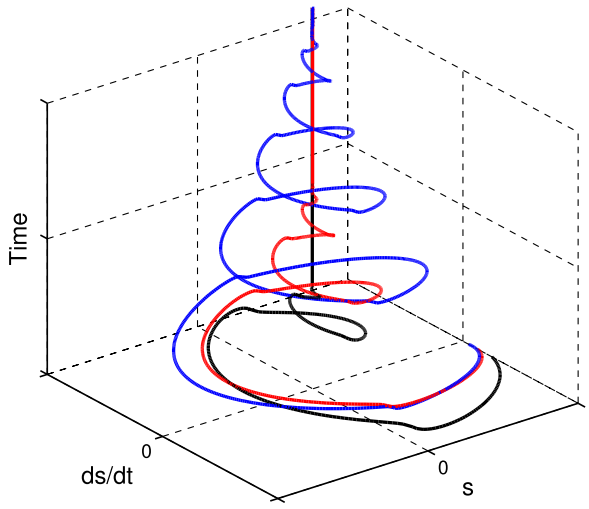

Fig. 1. STA trajectories.

IV. MRAS Speed Estimator Based on the ST-SOSM Observer

A. Conventional MRAS Scheme

Fig. 2 shows a block diagram of the conventional rotor-flux-based MRAS speed estimator [18]. The reference model (voltage model) is constructed by

$$\dot{\hat{\boldsymbol{\Psi}}}_s = -R_s \boldsymbol{i}_s + \boldsymbol{v}_s \tag{8}$$

$$\hat{\boldsymbol{\Psi}}_{rV} = \frac{L_r}{L_m}(\hat{\boldsymbol{\Psi}}_s - \sigma L_s \boldsymbol{i}_s) \tag{9}$$

where $\sigma = 1 - L_m^2/L_s L_r$ is the leakage coefficient, and the hat sign denotes the estimated values. The adjustable model (current model) is given by

$$\dot{\hat{\boldsymbol{\Psi}}}_{rC} = \frac{L_m}{T_r}\boldsymbol{i}_s - \left(\frac{1}{T_r} - j\hat{\omega}_r\right)\hat{\boldsymbol{\Psi}}_{rC} \tag{10}$$

where $T_r = L_r/R_r$ is the rotor time constant.

In the MRAS scheme, the stability analysis of the estimator is performed using Popov's hyperstability theorem, whereby the error equations of the estimated rotor fluxes must fulfill Popov's integral inequality [18]. Then, the adaptation law is deduced as (the proof can be found in [18] and [19])

$$\hat{\omega}_r = \left(K_p + \frac{K_i}{s}\right)\epsilon_\omega \tag{11}$$

where K_p and K_i are the proportional and integral gains, respectively, and ϵ_ω is the error quantity for the speed estimation, given as

$$\epsilon_\omega = \hat{\psi}_{r\alpha C}\hat{\psi}_{r\beta V} - \hat{\psi}_{r\beta C}\hat{\psi}_{r\alpha V}. \tag{12}$$

B. ST-SOSM Flux Observer Design

The performance of the DTC scheme is dramatically affected by the stator flux that is estimated using the reference model.

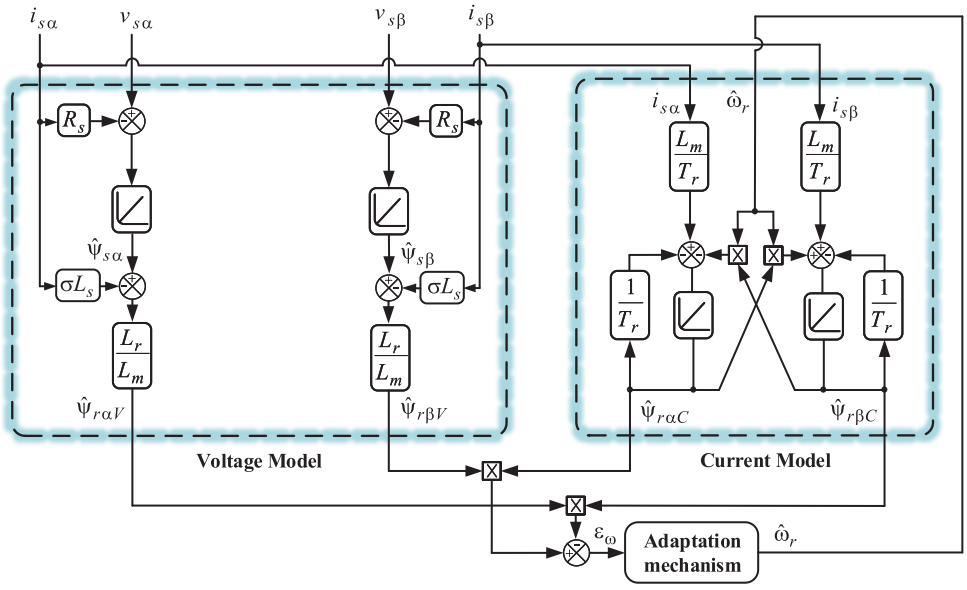

Fig. 2. Conventional rotor-flux-based MRAS-based speed estimator.

In addition, the accuracy of the speed estimation is strictly related to the reference model and its parameters. In this study, the reference model is replaced by an improved one that is obtained using the ST-SOSM technique. The proposed reference model is given by the following expression:

$$\dot{\hat{\psi}}_{s\alpha} = -R_s i_{s\alpha} + v_{s\alpha} - \Pi_{i\alpha} \tag{13}$$

$$\dot{\hat{\psi}}_{s\beta} = -R_s i_{s\beta} + v_{s\beta} - \Pi_{i\beta} \tag{14}$$

where $\Pi_{s\alpha}$ and $\Pi_{s\beta}$ are the injected signals. Using (7), these signals are specified as follows:

$$\Pi_{i\alpha} = -\lambda_{i\alpha}|e_{i\alpha}|^{0.5}\text{sign}\,(e_{i\alpha}) - \zeta_{i\alpha}\int \text{sign}\,(e_{i\alpha})dt \tag{15}$$

$$\Pi_{i\beta} = -\lambda_{i\beta}|e_{i\beta}|^{0.5}\text{sign}\,(e_{i\beta}) - \zeta_{i\beta}\int \text{sign}\,(e_{i\beta})dt \tag{16}$$

where $e_{i\alpha} = i_{s\alpha} - \hat{i}_{s\alpha}$, $e_{i\beta} = i_{s\beta} - \hat{i}_{s\beta}$, and $\lambda_{i\alpha}$, $\lambda_{i\beta}$, $\zeta_{i\alpha}$, and $\zeta_{i\beta}$ are the constant parameters of the STA. To reach (15) and (16) from (7), it is assumed that there is no bound on the algorithm because the constraint $|u| \leq U_M$ is always satisfied in a finite time by choosing appropriate constant parameters for the STA [34]. Furthermore, ρ is set to 0.5 for obtaining the maximum real sliding order [32].

The estimated stator currents are calculated as

$$\hat{i}_{s\alpha} = \frac{1}{\sigma L_s L_r}\left(L_r\hat{\psi}_{s\alpha} - L_m\hat{\psi}_{r\alpha V}\right) \tag{17}$$

$$\hat{i}_{s\beta} = \frac{1}{\sigma L_s L_r}\left(L_r\hat{\psi}_{s\beta} - L_m\hat{\psi}_{r\beta V}\right). \tag{18}$$

The finite-time convergence of the observer is proved by the geometrical approach [33], [34]. By assuming that the real system is in the form of (13) and (14) without injected signals and using (4), the dynamics of the estimation errors are written as

$$L_s\dot{e}_{i\alpha} = \Pi_{i\alpha} \tag{19}$$

$$L_s\dot{e}_{i\beta} = \Pi_{i\beta}. \tag{20}$$

If the states of the system are assumed to be bounded, an upper bound Γ can be considered for nominal part and uncertainties of the system. Accordingly, the corresponding sufficient conditions for the finite-time convergence of the observer are [34]

$$\zeta_{i\alpha} > \Gamma_{i\alpha}$$

$$\lambda_{i\alpha}^2 > \frac{2}{\zeta_{i\alpha} - \Gamma_{i\alpha}}\left(\frac{(1+q)(\Gamma_{i\alpha} + \zeta_{i\alpha})}{1-q}\right)^2 \tag{21}$$

where $0 < q < 1$. A similar expression can be written for the β-axis component of the 6PIM.

The block diagram of the proposed MRAS speed estimator based on the ST-SOSM technique is shown in Fig. 3. The compensated reference model is based on (13)–(18), and the adjustable model is built using (10). A PI regulator is used as the adaptation mechanism to estimate the angular speed by using the adaptation law described in (11).

V. Modified DTC of the 6PIM Based on the ST-SOSM Controller

A. DTC Scheme With Duty Cycle Control

There are $2^6 = 64$ switching states in a six-phase voltage-source inverter (VSI), where each switching state yields a voltage vector in the $\alpha - \beta$ and $z_1 - z_2$ subspaces, as shown in Fig. 4. The resultant voltage space vectors in the $\alpha - \beta$ subspace can be categorized into five groups: large vectors ($V_L = 0.64V_{\text{dc}}$, where V_{dc} denotes the dc-link voltage), single-medium vectors ($V_{\text{SM}} = 0.47V_{\text{dc}}$), double-medium vectors ($V_{\text{DM}} = 0.33V_{\text{dc}}$), small vectors ($V_S = 0.17V_{\text{dc}}$), and null vectors.

The block diagram of the switching-table-based DTC (ST-DTC) is shown in Fig. 5. In the ST-DTC, the required

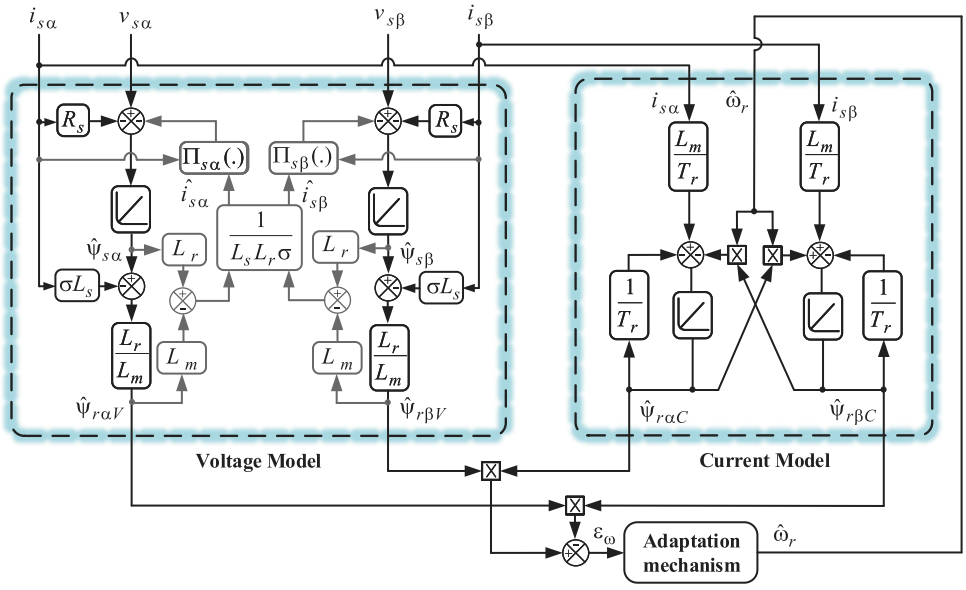

Fig. 3. Proposed MRAS estimator based on the ST-SOSM technique.

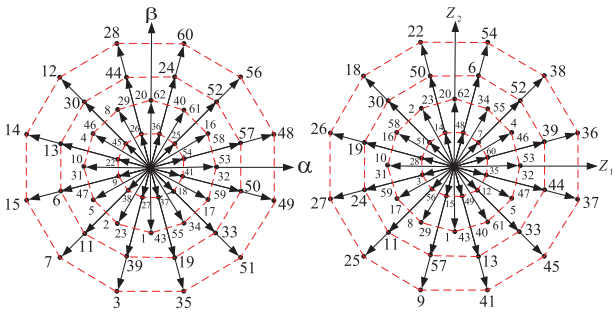

Fig. 4. Voltage space vectors of inverter in the $\alpha-\beta$ (left side) and the z_1-z_2 (right side) subspaces.

TABLE I
SWITCHING TABLE OF THE DTC STRATEGY

ϵ_T	ϵ_ψ	Selected voltage*
1	1	V_{m+1}
1	0	V_{m+4}
0	1	V_0
0	0	V_0
-1	1	V_{m-2}
-1	0	V_{m-5}

*m is sector number

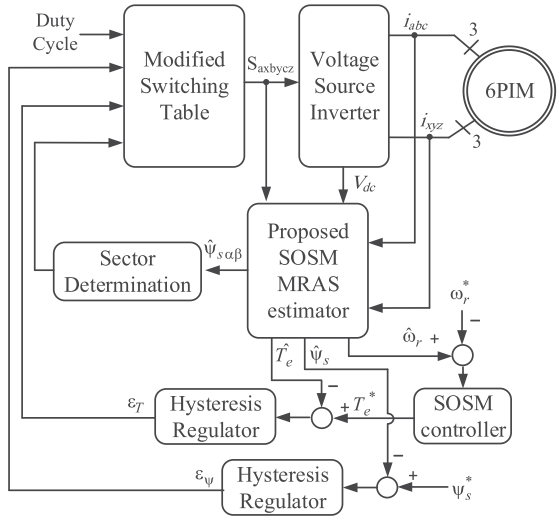

Fig. 5. Block diagram of the ST-DTC scheme.

voltage vector is usually selected from the large voltage vectors in the $\alpha-\beta$ subspace according to the torque control signal (ϵ_T), the stator flux control signal (ϵ_ψ), and the position of the stator flux using a switching table, as shown in Table I. The torque and stator flux control signals are obtained by three-level and two-level hysteresis regulators, respectively. The angular speed, stator flux, and electromagnetic torque of the 6PIM can be estimated using the proposed MRAS scheme. The speed control loop is based on the ST-SOSM controller, which is discussed in the next subsection. When applying only the large voltage vectors in the $\alpha-\beta$ subspace, the corresponding voltage vectors in the z_1-z_2 subspace produce low-order harmonics in the stator currents.

To reduce the current harmonics, the duty cycle control DTC is used in this paper, where virtual voltage vectors are applied to the motor during each sampling period. The virtual vectors are a combination of large voltage vectors V_L and its corresponding single-medium voltage vectors $V_{\rm SM}$. The reason lies in the fact that every pair of the V_L and $V_{\rm SM}$ vectors, located in the same sector in the $\alpha-\beta$ subspace, are in the opposite directions in the z_1-z_2 subspace (see Fig. 4). The vector durations can be determined based on a simple principle to reduce average volt–seconds in the z_1-z_2 subspace as follows:

$$\begin{cases} T_L \times V_L = T_{\rm SM} \times V_{\rm SM} \\ T_L + T_{\rm SM} = T_s \end{cases} \Rightarrow \begin{cases} T_L = 0.73T_s \\ T_{\rm SM} = 0.27T_s \end{cases} \tag{22}$$

where T_s, T_L, and $T_{\rm SM}$ are the sampling time, the large vector duration, and the single-medium vector duration, respectively.

The readers are encouraged to find more information and results about the duty cycle control in [38] and [39].

B. ST-SOSM Speed Controller Design

To replace the conventional PI controller in the speed control loop of the DTC of the 6PIM, which is faced with several problems [20], an ST-SOSM speed controller is designed here. The required sliding variable s_ω is defined as

$$s_\omega = \omega_r - \omega_r^* \tag{23}$$

where ω_r^* denotes the speed reference. The actual torque control law is proposed based on (7) in the following way:

$$T_a = -\lambda_{Te}|s_\omega|^{0.5}\text{sign}\,(s_\omega) - \zeta_{Te}\int \text{sign}\,(s_\omega)dt \tag{24}$$

where λ_{Te} and ζ_{Te} are the design parameters. Under sufficient conditions, this control law ensures that the sliding surface is reached in a finite time. Now, the control law needs a supplementary signal to ensure that the system trajectory stays on the sliding surface after termination of the reaching mode, which is usually referred to as the equivalent control law. For this purpose, an expression for the error dynamics is provided using the mechanical equations of the 6PIM as follows:

$$\dot{s}_\omega = \frac{P}{J}\left(T_e - T_L - \frac{B}{P}\omega_r\right) - \dot{\omega}_r^* \tag{25}$$

where B is the friction coefficient. During the sliding mode, the trajectories of the system are bounded in the manifold $s_\omega = \dot{s}_\omega = 0$ for $t > t_r$, where t_r is the reaching time. The equivalent control law is deduced by solving $\dot{s}_\omega = 0, t > t_r$ as

$$T_{\text{eq}} = \hat{T}_L + \frac{B}{P}\hat{\omega}_r. \tag{26}$$

Using (24) and (26), the toque control law is given by

$$T_e^* = T_a + T_{\text{eq}}. \tag{27}$$

In (27), the real parameters are substituted with the corresponding estimated parameters. As can be seen from (26), the equivalent control law is based on the load torque. Due to the problems with the torque transducers, especially the invasive procedure of their installation, the observation of the load torque is preferred. Therefore, a load torque observer is proposed based on the ST-SOSM technique.

C. ST-SOSM Load Torque Observer Design

Actually, the changes of the load torque in the time scale of the electrical quantities of the 6PIM can be neglected (i.e., $\dot{T}_L \approx 0$); hence, the load torque can be assumed as a quasi-constant quantity. In this section, a load torque observer is introduced based on the equivalent control method, which was beforehand used for the design of the speed controller. The proposed load torque observer is

$$\hat{T}_L = \frac{-J}{P}\zeta_\omega \int \text{sign}\,(e_\omega)dt \tag{28}$$

where $e_\omega = \hat{\omega}_r - \tilde{\omega}_r$, and $\tilde{\omega}_r$ is the auxiliary state of the rotor speed. This quantity is observed using the mechanical equation

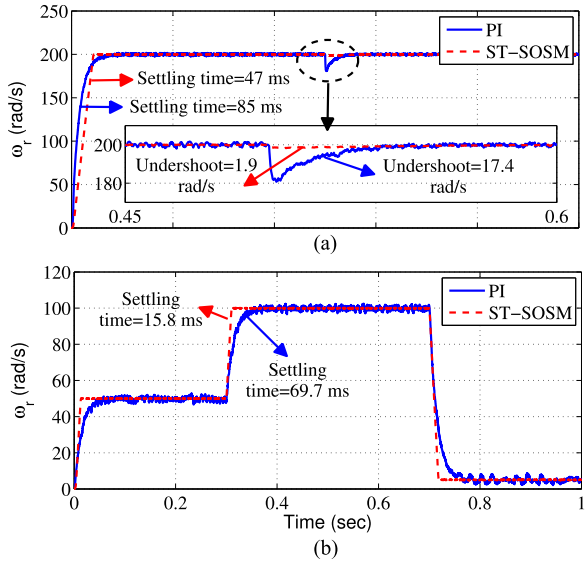

Fig. 6. Performance of the ST-SOSM and PI controllers under (a) change in the load torque and (b) changes in the speed.

of the 6PIM. Indeed, the load torque is obtained using the estimated rotor speed from the MRAS ($\hat{\omega}_r$) and the mechanical equations ($\tilde{\omega}_r$). The expression for $\tilde{\omega}_r$ is proposed as follows:

$$\dot{\tilde{\omega}}_r = \frac{P}{J}\hat{T}_e - \frac{B}{J}\tilde{\omega}_r - \Pi_\omega \tag{29}$$

where Π_ω is an injected signal to the observer as

$$\Pi_\omega = -\lambda_\omega|e_\omega|^{0.5}\text{sign}\,(e_\omega) - \zeta_\omega\int \text{sign}\,(e_\omega)dt \tag{30}$$

where λ_ω and ζ_ω are the design parameters of the STA. The error dynamics of the observer is

$$\dot{e}_\omega = -\frac{P}{J}\hat{T}_L - \frac{B}{J}e_\omega + \Pi_\omega. \tag{31}$$

Using similar inequalities as described by (21), the finite-time convergence of (31) is ensured under sufficient conditions, which are obtained from the geometrical settings.

VI. Simulation Results

The modified DTC scheme with the proposed ST-SOSM MRAS speed estimator and the load torque observer are simulated in MATLAB/Simulink for a 6PIM, whose technical specifications will be presented in the next section. The sampling frequency is chosen to be 10 kHz. The performance of the ST-SOSM controller, which is located in the speed control loop of the DTC scheme, is shown in Fig. 6. Fig. 6(a) depicts the results under the step change of the load torque from 0 to about 2 N·m at $t = 0.5$ s and a constant speed command of 200 rad/s. Fig. 6(b) presents the results under no load with $\omega_r^* = 50 \rightarrow 100 \rightarrow 5$ rad/s. The corresponding results obtained using the conventional PI controller are given in the figures as well. The simulation results confirm the higher robustness of the ST-SOSM controller against the external load torque disturbance and its faster dynamic response during the speed command changes.

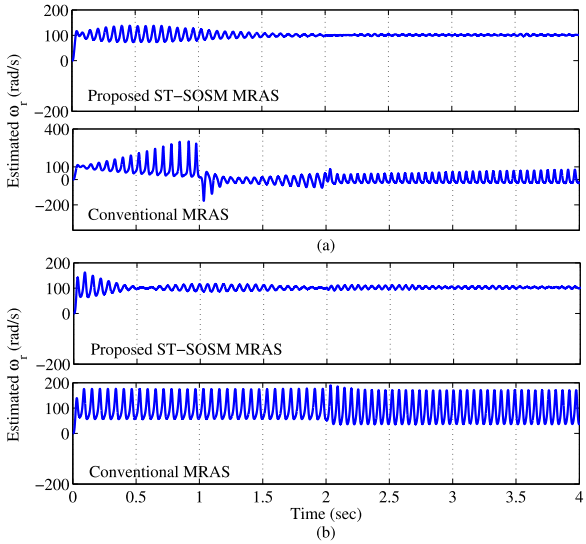

Fig. 7. Open-loop estimation of the speed with the proposed ST-SOSM and conventional MRAS-based speed estimator under (a) 300-mV dc-offset voltage and (b) 50% mismatch in R_s.

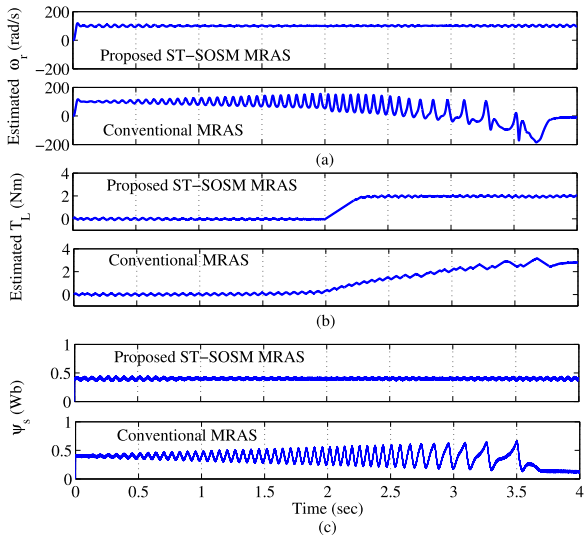

Fig. 8. Performance of the sensorless DTC with the proposed ST-SOSM and the conventional MRAS-based speed estimators under 50-mV dc-offset voltage for the (a) estimated speed, (b) estimated load torque, and (c) stator flux.

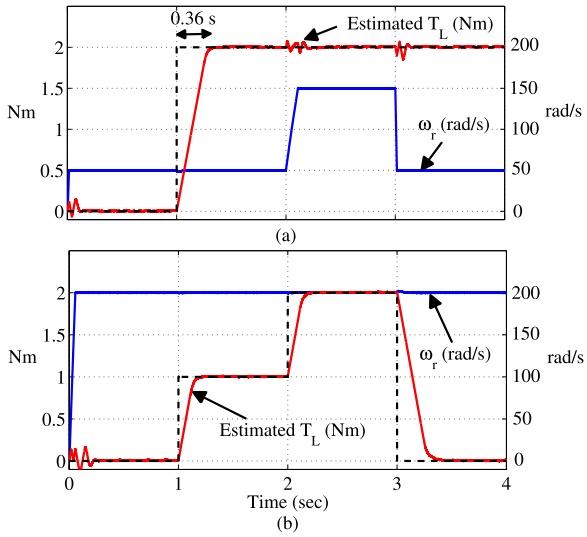

Fig. 9. Operation of the proposed ST-SOSM load torque observer under (a) changes in the speed and (b) changes in the load torque.

The dc offsets and the positive mismatch of the stator resistance (R_s) are two common problems that may occur in practice due to the open-loop integration and limited accuracy of the measurement transducers and the thermal drift, respectively. Under positive R_s mismatch ($\Delta R_s = R_s - \hat{R}_s > 0$), the tuned stator resistance in the controller ($\hat{R}_s$) is smaller than its actual value (R_s) in the 6PIM. The performance of the proposed ST-SOSM MRAS speed estimator is examined under the mentioned problems. The simulation results for the open-loop estimation of the rotor speed under the 300-mV dc offset (added to the $v_{s\alpha}$ and $v_{s\beta}$) and a 50% positive stator resistance mismatch are shown in Fig. 7(a) and (b), respectively, under a speed command of 100 rad/s. In the open-loop estimation, the estimated quantity is not applied in the simulation process, but it is merely to show the estimation accuracy. From the figures, it is clear that the conventional MRAS is fully degraded by the dc offset and the stator resistance mismatch problems, while the proposed ST-SOSM scheme provides robust performance due to the injected terms into the voltage model of the 6PIM.

The sensorless operation of the DTC scheme with the proposed ST-SOSM and the conventional MRAS speed estimator under the 50-mV dc offset in the voltage components for the estimated speed, load torque, and stator flux is shown in Fig. 8(a)–(c), respectively. In this test, the speed command is 100 rad/s, the load torque changes as a step function from 0 to 2 N·m at $t = 2$ s, and the flux command is 0.4 Wb. It can be clearly adjudged that the reference tracking is gradually lost in the conventional MRAS, which is due to the pure integration of the asymmetric stator voltages. However, the proposed ST-SOSM MRAS speed estimator has a robust operation against the dc-offset problem in the sensorless mode.

The simulation results for evaluating the performance of the proposed ST-SOSM load torque observer under a constant load torque and step changes in the speed are shown in Fig. 9(a), while the results under the constant speed and changes in the load torque are illustrated in Fig. 9(b). It can be seen that the load torque observer is capable to track its real value under different scenarios. It is worth mentioning here that the estimated load torque has an important role in the equivalent control law of the speed loop.

VII. Experimental Validation

In addition to the simulation results, the performance of the proposed scheme is validated by extensive experiments. The sampling frequency is 10 kHz with a dead band of 2 μs. The experimental data are captured using data acquisition card and serial port with LABVIEW and MATLAB software, respectively. The serial communication interface module is used to provide a serial connection between the host PC and the DSP board.

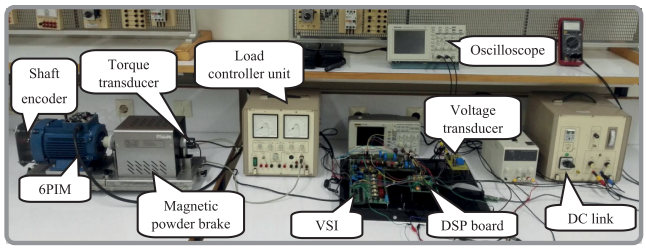

Fig. 10. Photograph of the experimental setup.

TABLE II
PARAMETERS OF THE 6PIM

Symbol	Quantity	Value
P	Pole pairs	1
R_s	Stator resistance	4.08 Ω
R_r	Rotor resistance	3.73 Ω
L_s	Stator inductance	443.6 mH
L_r	Rotor inductance	443.6 mH
L_m	Magnetizing inductance	429.8 mH
J	Moment of inertia	0.000718 $kg.m^2$

A. Test Bench Description

The photograph of the experimental setup is shown in Fig. 10. It consists of the following main elements:

1) a DSP board based on the floating-point TMS320F28335 processor;
2) tailor-made three-phase VSIs with BUP 314D insulated-gate bipolar transistors, HCPL-316J gate drivers, 6N137 optocouplers, MAU 209, 302 dc–dc converter, and LEM LTS 6-NP current transducers;
3) LEM LV25-P voltage transducer;
4) Autonics incremental shaft encoder with a resolution of 2500 pulses/revolution;
5) magnetic powder brake and its controller unit;
6) torque transducer based on strain gauge;
7) single-phase rectifier bridge and the dc link; and
8) a 1-hp 24-stator-slot three-phase squirrel-cage induction motor, which has been rewound to construct a two-pole asymmetrical 6PIM.

The parameters of the 6PIM are tabulated in Table II.

B. Steady-State and Dynamic Performance of the Proposed Sensorless DTC Scheme

The steady-state performance of the proposed sensorless DTC scheme for the estimated speed, stator flux, electromagnetic torque, and estimated load torque is shown in Fig. 11(a). The corresponding current waveforms, including the stator phase current, the α-component of the currents, and the z_1-component of the currents, are also shown in Fig. 11(b). In this test, the speed and flux commands are set to 150 rad/s and 0.4 Wb, respectively, and the load torque is 2 N·m. This figure confirms the good tracking, observing, and estimating capabilities of the proposed ST-SOSM speed controller, MRAS speed estimator, and load torque observer, respectively.

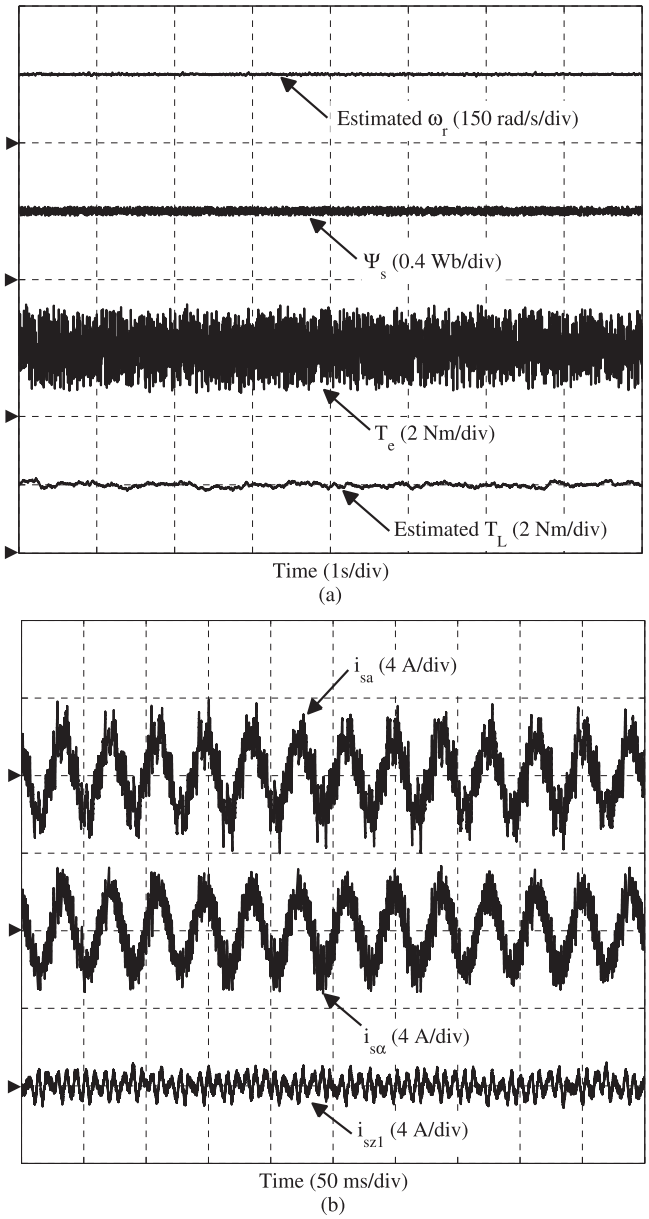

Fig. 11. Steady-state response of the proposed sensorless DTC scheme for the (a) speed, stator flux, electromagnetic torque, and estimated load torque and (b) corresponding current waveforms.

The dynamic performance of the sensorless DTC scheme is investigated by the step change of the speed command from 5 to 100 rad/s under zero load torque. The experimental results captured through this test are depicted in Fig. 12. The results confirm the effectiveness of the proposed ST-SOSM MRAS speed estimator from low speed (1.7% rated speed) to middle speed (34 % rated speed) and also the load torque observer under the no-load condition. The speed overshoot is 2.6 rad/s, which is rather small (2.6% command speed), and the settling time is near to 0.71 s.

To evaluate the disturbance-free operation of the ST-SOSM speed controller, its performance is compared with the PI speed controller. The comparison of the actual speed attained through the ST-SOSM and the PI speed controllers at 4.8% rated speed

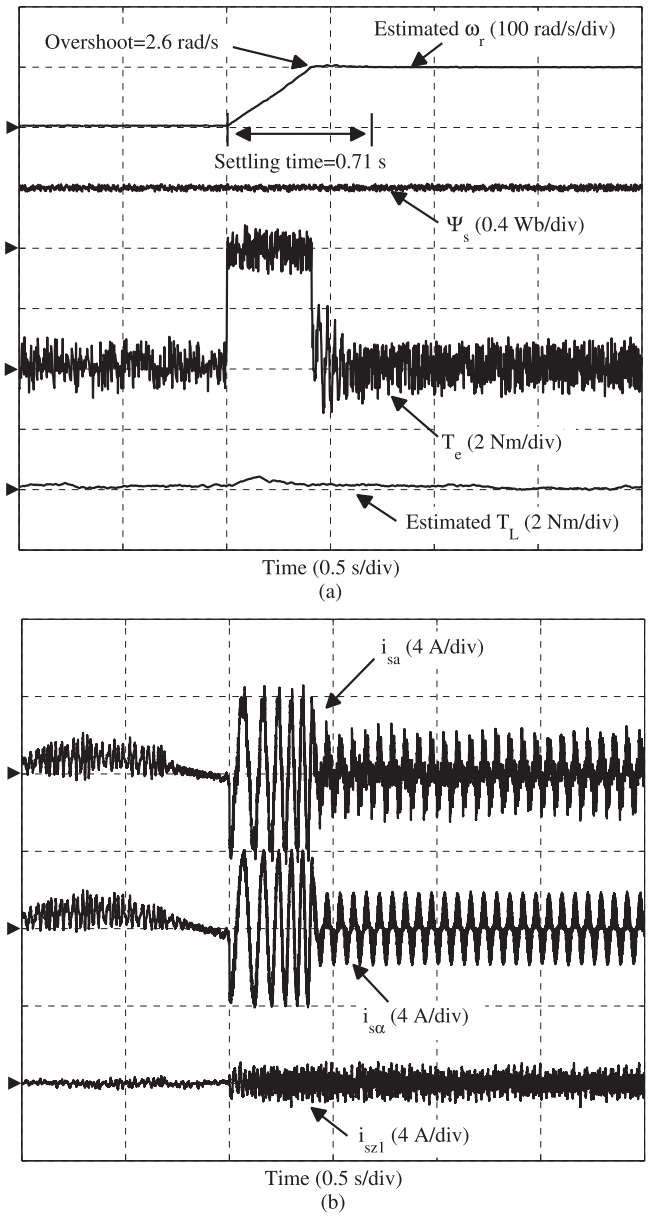

Fig. 12. Dynamic response of the proposed sensorless DTC scheme for the (a) speed, stator flux, electromagnetic torque, and estimated load torque and (b) corresponding current waveforms.

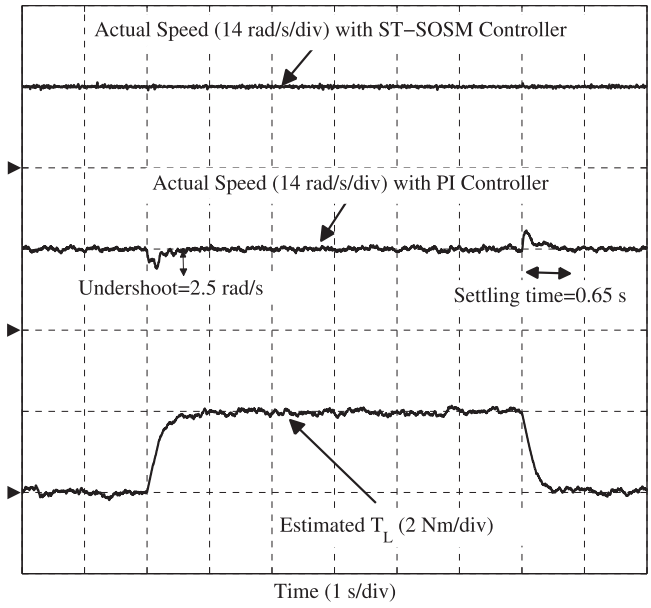

Fig. 13. Performance of the ST-SOSM speed controller in comparison with the PI controller under step changes of the load torque.

and step changes of the load torque from 0 to 2 N·m is available in Fig. 13. It can be seen that applying the load torque to the motor leads to a 17.8% undershoot (overshoot) of the speed, when the PI controller is used. However, the ST-SOSM speed controller is robust against such external disturbances. This is because the control law of the ST-SOSM technique is compensated by the estimated load torque.

C. Performance of the Proposed Speed Estimator

To confirm the effectiveness of the proposed ST-SOSM MRAS speed estimator presented in Fig. 3, various experiments have been performed under different operating conditions, mainly focusing on the low-speed region (0–2.5 Hz),

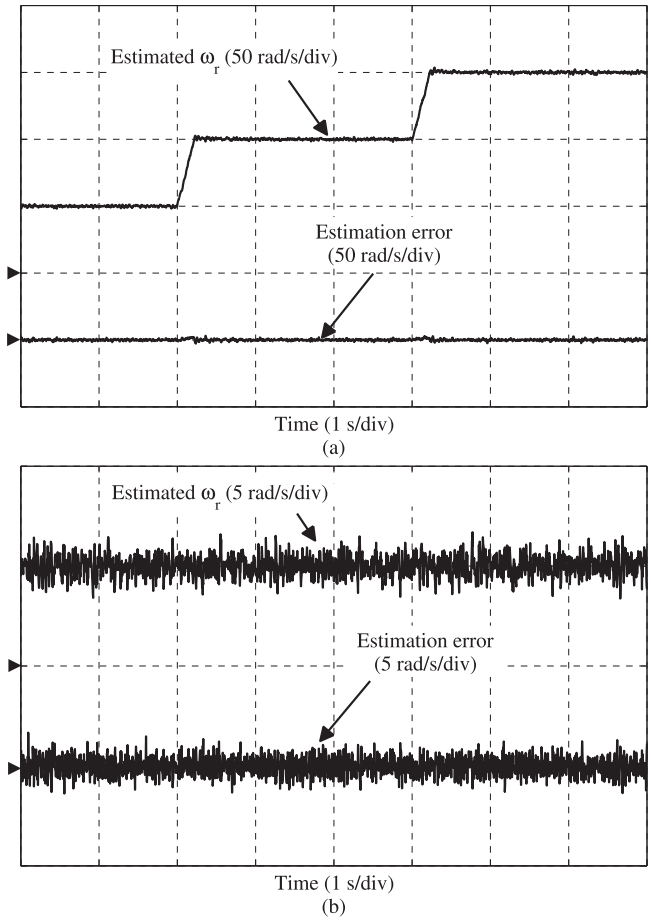

Fig. 14. Performance of the proposed ST-SOSM MRAS speed estimator for the estimated speed and estimation error under the no-load condition and changes in (a) speed and (b) low speed.

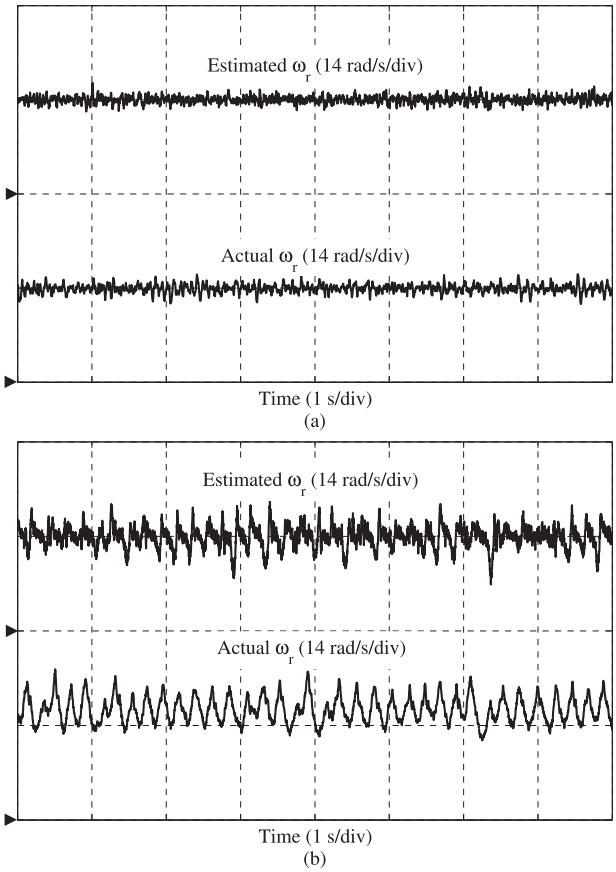

Fig. 15. Performance of the (a) proposed and (b) conventional MRAS strategies for a 20% stator resistance mismatch.

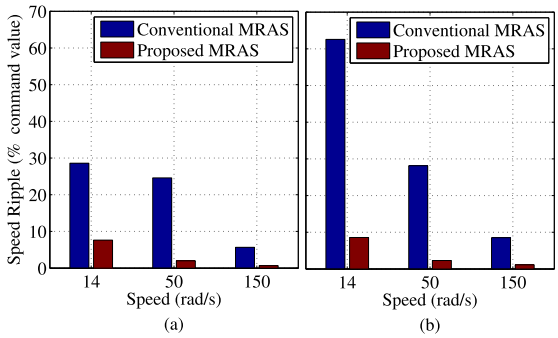

Fig. 16. Comparison of the speed ripples due to (a) 10% and (b) 30% stator resistance mismatch at different speeds and the rated load torque.

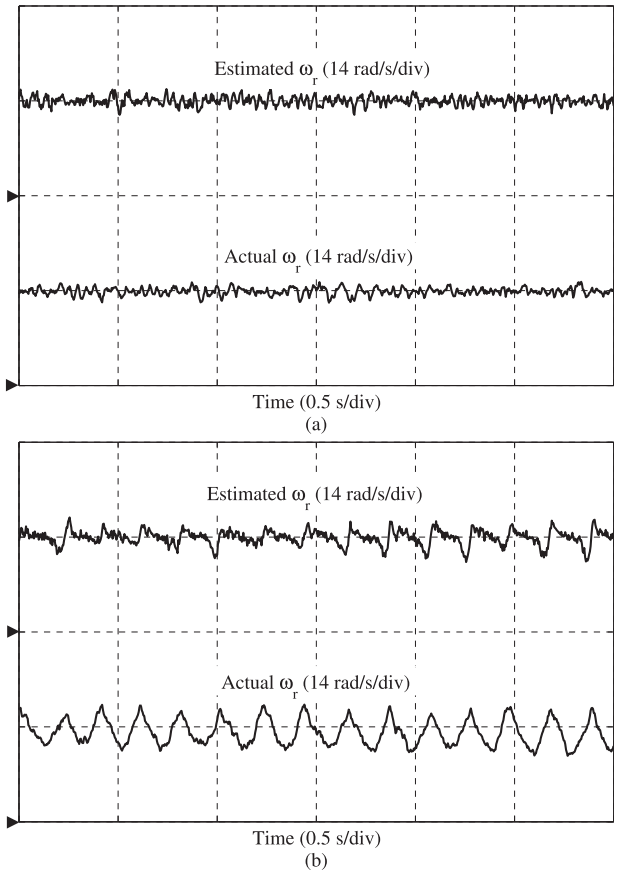

Fig. 17. Performance of the (a) proposed and (b) conventional MRAS strategies for an intentionally introduced dc offset in the stator current components.

which is more critical for the correct operation of the sensorless drive systems. The estimated speed and its error under the no-load condition are shown in Fig. 14. In the first test, the speed command is changed from 50 to 100 and then to 150 rad/s, while in the second test, the speed command is constant. From Fig. 14(a), it can be realized that the estimation error is about zero except for short time durations around the speed command changes. Fig. 14(b) depicts that the estimation error remains close to zero for the speed command that is as low as 5 rad/s.

As discussed previously, the stator resistance mismatch and the dc offset can lead to a degraded performance of the conventional MRAS estimator and DTC strategies. A positive R_s mismatch ($\Delta R_s > 0$) in the sensorless DTC strategy causes erroneous estimation of the flux and torque. Under this condition, the actual flux of the motor will be lower than its command value [40], the tracking of the actual speed will be lost, and the real and estimated speeds encounter undesired oscillations. In [23], some experimental results have been presented for demonstrating the oscillations of the speed response due to the uncertainties of the parameters in the MRAS strategy. For a negative R_s mismatch ($\Delta R_s < 0$), the DTC drive system will be unstable [40] by severe oscillations of the stator flux and torque. The dc offset in the stator phase currents causes oscillations on the speed and the actual flux, where the magnitude of the oscillations can grow until instability of the drive system. The instability brings the motor into the saturation, where the flux, torque, and speed encounter severe oscillations.

The performances of the proposed ST-SOSM and the conventional MRAS speed estimators for a 20% positive stator resistance mismatch are shown in Fig. 15(a) and (b), respectively. These tests are performed at a 4.8% rated speed (14 rad/s) and a rated load torque (2 N·m). It is obvious that the proposed MRAS scheme operates robustly against the stator resistance mismatch, whereas the operation of the conventional MRAS strategy is completely degraded by it. Poor operation of the conventional MRAS strategy due to the R_s mismatch worsens at low speeds and high load torques, where the back electromotive force decreases and becomes comparable with the voltage drop across R_s. The speed ripples under 10% and 30% stator resistance mismatch are compared in Fig. 16 for the proposed

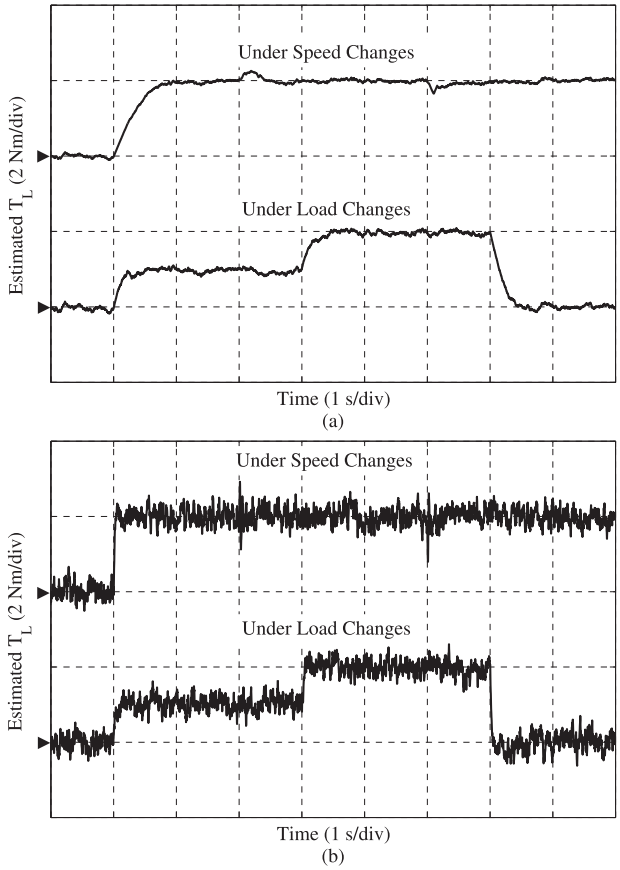

Fig. 18. Performance of the (a) proposed ST-SOSM and (b) conventional FOSM load torque observers under speed changes and load changes.

and conventional MRAS speed estimators. Obviously, a larger R_s mismatch at lower speed leads to a larger speed ripple for the conventional MRAS estimator, while the proposed MRAS strategy is marginally affected by the R_s mismatch.

The dc offsets are inherently occurred in the measurements of the voltages and currents, and their magnitudes depend on the temperature. The estimated and actual speeds within a short-time frame for the proposed and conventional MRAS speed estimators with an intentionally introduced dc offset in the stator current components are shown in Fig. 17(a) and (b), respectively. The offset-free estimating capability of the proposed ST-SOSM MRAS estimator is clearly observed in this test.

D. Performance of the Proposed Load Torque Observer

In this section, the performance of the proposed ST-SOSM load torque observer is investigated under changing the speed and the load torque. The experimental results of the estimated load torque for the proposed ST-SOSM and conventional FOSM load torque observers are shown in Fig. 18(a) and (b), respectively. The results have been depicted for two different scenarios. In the first scenario (speed changes), the speed command changes from 50 to 150 and back to 50 rad/s at $t = 0$, 3, and 6 s, respectively, under a constant load torque of 2 N·m. In the second scenario (load changes), the load torque changes as $T_L = 0 \rightarrow 1 \rightarrow 2 \rightarrow 0$ N·m at $t = 0 \rightarrow 1 \rightarrow 4 \rightarrow 7$ s under a constant speed of 200 rad/s. From the depicted results, it is evident that the proposed ST-SOSM load torque observer can provide the load torque with an acceptable quality, whereas the conventional FOSM observer is remarkably affected by the chattering problem.

VIII. Conclusion

In this paper, a novel MRAS speed estimator has been proposed using a ST-SOSM strategy for sensorless DTC of 6PIMs. A modified version of the reference model was introduced to increase the robustness of the MRAS scheme against the dc offsets and the stator resistance mismatches. The finite-time convergence of the proposed ST-SOSM algorithm was approved using the geometrical approach. Various simulation and experimental results confirmed the robustness and effectiveness of the proposed speed estimation system under different operating conditions. An ST-SOSM controller was introduced using the equivalent control method for eliminating the PI regulator and its related drawbacks from the speed control loop of the DTC scheme. The simulation and experimental results verified better performance of the ST-SOSM speed controller compared with the PI regulator from the viewpoints of dynamic behavior and robustness against the external disturbances. Finally, a load torque observer was proposed using the ST-SOSM strategy and the equivalent control method to be used in the speed control loop. The load torque observer was tested under various operating conditions and compared with the conventional FOSM load torque observer to verify its efficiency.

References

[1] M. J. Duran, I. Gonzalez-Prieto, N. Rios-Garcia, and F. Barrero, "A simple, fast, and robust open-phase fault detection technique for six-phase induction motor drives," *IEEE Trans. Power Electron.*, vol. 33, no. 1, pp. 547–557, Jan. 2018.

[2] M. Bermudez, I. Gonzalez-Prieto, F. Barrero, H. Guzman, X. Kestelyn, and M. J. Duran, "An experimental assessment of open-phase fault-tolerant virtual-vector-based direct torque control in five-phase induction motor drives," *IEEE Trans. Power Electron.*, vol. 33, no. 3, pp. 2774–2784, Mar. 2018.

[3] H. S. Che, M. J. Duran, E. Levi, M. Jones, W. P. Hew, and N. A. Rahim, "Postfault operation of an asymmetrical six-phase induction machine with single and two isolated neutral points," *IEEE Trans. Power Electron.*, vol. 29, no. 10, pp. 5406–5416, Oct. 2014.

[4] A. Tani, M. Mengoni, L. Zarri, G. Serra, and D. Casadei, "Control of multiphase induction motors with an odd number of phases under open-circuit phase faults," *IEEE Trans. Power Electron.*, vol. 27, no. 2, pp. 565–577, Feb. 2012.

[5] A. S. Abdel-Khalik, M. S. Hamad, A. M. Massoud, and S. Ahmed, "Postfault operation of a nine-phase six-terminal induction machine under single open-line fault," *IEEE Trans. Ind. Electron.*, vol. 65, no. 2, pp. 1084–1096, Feb. 2018.

[6] E. Levi, M. Jones, and S. N. Vukosavic, "A series-connected two-motor six-phase drive with induction and permanent magnet machines," *IEEE Trans. Energy Convers.*, vol. 21, no. 1, pp. 121–129, Mar. 2006.

[7] H. S. Che, E. Levi, M. Jones, W. P. Hew, and N. A. Rahim, "Current control methods for an asymmetrical six-phase induction motor drive," *IEEE Trans. Power Electron.*, vol. 29, no. 1, pp. 407–417, Jan. 2014.

[8] M. J. Duran, I. Gonzalez-Prieto, F. Barrero, E. Levi, L. Zarri, and M. Mengoni, "A simple braking method for six-phase induction motor drives with unidirectional power flow in the base-speed region," *IEEE Trans. Ind. Electron.*, vol. 64, no. 8, pp. 6032–6041, Aug. 2017.

[9] M. H. Holakooie, A. Taheri, and M. B. Sharifian, "MRAS based speed estimator for sensorless vector control of a linear induction motor with improved adaptation mechanisms," *J. Power Electron.*, vol. 15, no. 5, pp. 1274–1285, 2015.

[10] J. Holtz, "Sensorless control of induction machines—With or without signal injection?" *IEEE Trans. Ind. Electron.*, vol. 53, no. 1, pp. 7–30, Feb. 2006.
[11] W. Sun, Y. Yu, G. Wang, B. Li, and D. Xu, "Design method of adaptive full order observer with or without estimated flux error in speed estimation algorithm," *IEEE Trans. Power Electron.*, vol. 31, no. 3, pp. 2609–2626, Mar. 2016.
[12] M. H. Holakooie, M. Ojaghi, and A. Taheri, "Full-order Luenberger observer based on fuzzy-logic control for sensorless field-oriented control of a single-sided linear induction motor," *ISA Trans.*, vol. 60, pp. 96–108, 2016.
[13] R. P. Vieira, C. C. Gastaldini, R. Z. Azzolin, and H. A. Grundling, "Sensorless sliding-mode rotor speed observer of induction machines based on magnetizing current estimation," *IEEE Trans. Ind. Electron.*, vol. 61, no. 9, pp. 4573–4582, Sep. 2014.
[14] S. D. Gennaro, J. R. Dominguez, and M. A. Meza, "Sensorless high order sliding mode control of induction motors with core loss," *IEEE Trans. Ind. Electron.*, vol. 61, no. 6, pp. 2678–2689, Jun. 2014.
[15] S. A. Davari, D. A. Khaburi, F. Wang, and R. M. Kennel, "Using full order and reduced order observers for robust sensorless predictive torque control of induction motors," *IEEE Trans. Power Electron.*, vol. 27, no. 7, pp. 3424–3433, Jul. 2012.
[16] Z.-g. Yin, C. Zhao, Y.-R. Zhong, and J. Liu, "Research on robust performance of speed-sensorless vector control for the induction motor using an interfacing multiple-model extended Kalman filter," *IEEE Trans. Power Electron.*, vol. 29, no. 6, pp. 3011–3019, Jun. 2014.
[17] M. Barut, R. Demir, E. Zerdali, and R. Inan, "Real-time implementation of bi input-extended Kalman filter-based estimator for speed-sensorless control of induction motors," *IEEE Trans. Ind. Electron.*, vol. 59, no. 11, pp. 4197–4206, Nov. 2012.
[18] C. Schauder, "Adaptive speed identification for vector control of induction motors without rotational transducers," *IEEE Trans. Ind. Appl.*, vol. 28, no. 5, pp. 1054–1061, Sep./Oct. 1992.
[19] V. Vasic, S. N. Vukosavic, and E. Levi, "A stator resistance estimation scheme for speed sensorless rotor flux oriented induction motor drives," *IEEE Trans. Energy Convers.*, vol. 18, no. 4, pp. 476–483, Dec. 2003.
[20] S. M. Gadoue, D. Giaouris, and J. W. Finch, "MRAS sensorless vector control of an induction motor using new sliding-mode and fuzzy-logic adaptation mechanisms," *IEEE Trans. Energy Convers.*, vol. 25, no. 2, pp. 394–402, Jun. 2010.
[21] H. B. Azza, N. Zaidi, M. Jemli, and M. Boussak, "Development and experimental evaluation of a sensorless speed control of SPIM using adaptive sliding mode-MRAS strategy," *IEEE J. Emerg. Sel. Topics Power Electron.*, vol. 2, no. 2, pp. 319–328, Jun. 2014.
[22] K. Wang, W. Yao, K. Lee, and Z. Lu, "Regenerating mode stability improvements for combined voltage and current mode flux observer in speed sensorless induction machine control," *IEEE Trans. Ind. Appl.*, vol. 50, no. 4, pp. 2564–2573, Jul./Aug. 2014.
[23] A. Pal, S. Das, and A. K. Chattopadhyay, "An improved rotor flux space vector based MRAS for field oriented control of induction motor drives," *IEEE Trans. Power Electron.*, vol. 33, no. 6, pp. 5131–5141, Jun. 2018.
[24] A. V. R. Teja, V. Verma, and C. Chakraborty, "A new formulation of reactive-power-based model reference adaptive system for sensorless induction motor drive," *IEEE Trans. Ind. Electron.*, vol. 62, no. 11, pp. 6797–6808, Nov. 2015.
[25] A. K. Abdelsalam, M. I. Masoud, M. S. Hamad, and B. W. Williams, "Improved sensorless operation of a CSI-based induction motor drive: Long feeder case," *IEEE Trans. Power Electron.*, vol. 28, no. 8, pp. 4001–4012, Aug. 2013.
[26] E. Levi and M. Wang, "A speed estimator for high performance sensorless control of induction motors in the field weakening region," *IEEE Trans. Power Electron.*, vol. 17, no. 3, pp. 365–378, May 2002.
[27] F. Wang *et al.*, "Finite control set model predictive torque control of induction machine with a robust adaptive observer," *IEEE Trans. Ind. Electron.*, vol. 64, no. 4, pp. 2631–2641, Apr. 2017.
[28] L. Zhao, J. Huang, H. Liu, B. Li, and W. Kong, "Second-order sliding-mode observer with online parameter identification for sensorless induction motor drives," *IEEE Trans. Ind. Electron.*, vol. 61, no. 10, pp. 5280–5289, Oct. 2014.
[29] K. Akatsu and A. Kawamura, "Online rotor resistance estimation using the transient state under the speed sensorless control of induction motor," *IEEE Trans. Power Electron.*, vol. 15, no. 3, pp. 553–560, May 2000.
[30] Z. Xu and M. F. Rahman, "Comparison of a sliding observer and a Kalman filter for direct-torque-controlled IPM synchronous motor drives," *IEEE Trans. Ind. Electron.*, vol. 59, no. 11, pp. 4179–4188, Nov. 2012.
[31] V. Utkin, J. Guldner, and J. Shi, *Sliding Mode Control in Electro-Mechanical Systems*, 2nd ed. New York, NY, USA: Taylor & Francis, 2009.
[32] A. Levant, "Sliding order and sliding accuracy in sliding mode control," *Int. J. Control*, vol. 58, no. 6, pp. 1247–1263, 1993.
[33] A. Levant, "Principles of 2-sliding mode design," *Automatica*, vol. 43, no. 4, pp. 576–586, 2007.
[34] Y. Shtessel, C. Edwards, L. Fridman, and A. Levant, *Sliding Mode Control and Observation*, 1st ed. Basel, Switzerland: Birkhäuser, 2014.
[35] O. Barambones and P. Alkorta, "Position control of the induction motor using an adaptive sliding-mode controller and observers," *IEEE Trans. Ind. Electron.*, vol. 61, no. 12, pp. 6556–6565, Dec. 2014.
[36] Y. Zhao and T. A. Lipo, "Space vector PWM control of dual three-phase induction machine using vector space decomposition," *IEEE Trans. Ind. Appl.*, vol. 31, no. 5, pp. 1100–1109, Sep./Oct. 1995.
[37] J. A. Moreno and M. Osorio, "Strict Lyapunov functions for the super-twisting algorithm," *IEEE Trans. Automat. Control*, vol. 57, no. 4, pp. 1035–1040, Apr. 2012.
[38] L. Zheng, J. E. Fletcher, B. W. Williams, and X. He, "A novel direct torque control scheme for a sensorless five-phase induction motor drive," *IEEE Trans. Ind. Electron.*, vol. 58, no. 2, pp. 503–513, Feb. 2011.
[39] J. K. Pandit, M. V. Aware, R. V. Nemade, and E. Levi, "Direct torque control scheme for a six-phase induction motor with reduced torque ripple," *IEEE Trans. Power Electron.*, vol. 32, no. 9, pp. 7118–7129, Sep. 2017.
[40] G. Buja and R. Menis, "Steady-state performance degradation of a DTC IM drive under parameter and transduction errors," *IEEE Trans. Ind. Electron.*, vol. 55, no. 4, pp. 1749–1760, Apr. 2008.

Mohammad Hosein Holakooie was born in Tehran, Iran, in 1989. He received the B.Sc. degree from Guilan University, Rasht, Iran, in 2011, and the M.Sc. degree from the University of Tabriz, Tabriz, Iran, in 2013, both in electrical engineering. He is currently working toward the Ph.D. degree in electrical engineering with the University of Zanjan, Zanjan, Iran.

His current research interests include analysis and control of rotary and linear electric machines.

Mansour Ojaghi (S'05–M'10–SM'17) received the B.Sc. degree from the Shahid Chamran University of Ahwaz, Ahwaz, Iran, in 1993, the M.Sc. degree from the University of Tabriz, Tabriz, Iran, in 1997, and the Ph.D. degree from the University of Tehran, Tehran, Iran, in 2009, all in electrical engineering.

He was with the Zanjan Regional Electricity Company for ten years, where he was a Manager of the Grid Technical Office. After receiving the Ph.D. degree, he joined the Department of Electrical Engineering, University of Zanjan, Zanjan, Iran, where he is currently an Associate Professor. His research interests include modeling, simulation, and fault diagnosis of electrical machines and drives, as well as the power system protection.

Dr. Ojaghi is a Member of the IEEE Power and Energy Society, the IEEE Industrial Electronics Society, and the IEEE Industry Applications Society.

Asghar Taheri was born in Zanjan, Iran, in 1977. He received the B.S. and M.S. degrees from the Amirkabir University of Technology, Tehran, Iran, in 1999 and 2001, respectively, and the Ph.D. degree from the Iran University of Science and Technology, Tehran, in 2011, all in electronics engineering.

Since 2010, he has been a Faculty Member with the University of Zanjan, Zanjan, where he was an Assistant Professor from 2011 to 2016 and has been an Associate Professor since 2016. His current research interests include modeling, analysis, and control of power converters, motor drives and control, multiphase machine drives, multilevel inverters, power electronic systems for renewable energy sources, process control, digital-signal-processing- and field-programmable-gate-array-based system designs, hardware in the loop, and computer-aided control.